POLITECNICO DI TORINO
Repository ISTITUZIONALE

Lychee-like Bi2MoO6 Spheres for Highly Sensitive Room-Temperature Phosphine Sensing

Original
Lychee-like Bi2MoO6 Spheres for Highly Sensitive Room-Temperature Phosphine Sensing / He, X., Xu, J., Bian, Y., Tulliani, J., Zhang, C.. - In: ACS SENSORS. - ISSN 2379-3694. - 10:4(2025), pp. 2617-2626. [10.1021/acssensors.4c03135]

Availability:
This version is available at: 11583/3012430 since: 2026-06-25T15:28:57Z

Publisher:
American Chemical Society - ACS

Published
DOI:10.1021/acssensors.4c03135

Terms of use:

This article is made available under terms and conditions as specified in the corresponding bibliographic description in the repository

Publisher copyright
ACS postprint/Author's Accepted Manuscript

This document is the Accepted Manuscript version of a Published Work that appeared in final form in ACS SENSORS, copyright © American Chemical Society after peer review and technical editing by the publisher. To access the final edited and published work see http://dx.doi.org/10.1021/acssensors.4c03135.

(Article begins on next page)

02 July 2026

Lychee-like Bi_2MoO_6 Spheres for Highly Sensitive Room-Temperature Phosphine Sensing

Xiaoxi He[1,2], Jinyong Xu[1], Yixiang Bian[1], Jean-Marc Tulliani[2], Chao Zhang[1,]*

[1]College of Mechanical Engineering, Yangzhou University, Yangzhou 225127, China.

[2]Department of Applied Science and Technology, Politecnico di Torino, Torino 10129, Italy

Corresponding author
Prof. Chao Zhang
College of Mechanical Engineering
Key Laboratory of Surface Strengthening and Functional Manufacturing
Yangzhou University
Huayang West Road 196
Yangzhou 225127, Jiangsu Province
P.R. China
Tel/Fax: +86-514-87436008
Email: zhangc@yzu.edu.cn

ABSTRACT

The increasing use of phosphine in various industries demands the development of reliable sensors. However, progress in this area has been slow, particularly for room-temperature detection. In this study, bismuth molybdate microspheres with lychee-like structure (*Lyc-Bi_2MoO_6*) were prepared via a one-step solvothermal method, which can be employed for the detection of trace concentrations of phosphine. The solvent used was a mixture of isopropanol and ethylene glycol in a 3:1 ratio. Various characterization techniques and gas sensing performance tests demonstrated that *Lyc-Bi_2MoO_6* is a potential phosphine sensing material for room temperature application. Sensing performance tests revealed that *Lyc-Bi_2MoO_6* exhibited an impressive ability to detect trace concentrations of phosphine, with a practical detection limit as low as 150 ppb (response=8.11), rapid response (around 1 minute), and excellent long-term stability (a maximum response attenuation of 9.46% over 10 weeks). Density functional theory calculations further aided in the in-depth analysis and interpretation of the behavior and response mechanism of phosphine on the surface of *Lyc-Bi_2MoO_6*.

Keywords: Gas sensor; semiconductor; Bi_2MoO_6; lychee-like structure; phosphine; theoretical calculation

Phosphine (PH_3) is a highly toxic, colorless, and odorless gas. In recent years, it has not only been widely used in fumigation for agricultural storage and chemical synthesis but has also found extensive application in the manufacturing of semiconductor devices.[1–4] However, to date, no satisfactory development of ppm-level PH_3 detection technology has been achieved, and the test tube remains the most commonly used PH_3 detecting method, carrying all the disadvantages of manual operation. Monitoring the concentration of PH_3 during fumigation processes is crucial for confirming that the treatment is sufficient to achieve the desired insect control, but such monitoring can be relatively expensive and labor-intensive.[5,6] The fabrication of novel PH_3 sensing materials aids in the advancement of distributed sensor technology, improving the detection of concentration variations at different points during the fumigation process.[7] Simultaneously, it helps prevent excessive human exposure to PH_3, which can lead to severe consequences such as respiratory damage, headaches, pulmonary edema, and even death.[3,8] Occupational Safety and Health Administration (OSHA) has established a permissible exposure limit of 300 ppb for phosphine, with a short-term exposure limit of 1 ppm and National Institute for Occupational Safety and Health (NIOSH) has set the immediately dangerous to health exposure limit at 50 ppm. Semiconductor oxides have been extensively employed in the detection of various gases due to the growing demand for toxic gas sensors driven by safety and environmental protection concerns.[9–11] As early as the 1990s, Varfolomeev *et al.*,[12] Eguchi *et al.*,[13] Ratcheva *et al.*,[14] and Perez *et al.*[15] began developing semiconductor-based PH_3 sensors utilizing materials such as SnO_2-ZnO, $CaFeO_{2.5}$, SnO_2-ZrO_2, and N-octadecyl-pyridinium$^+$-Tetracyanoquinodimethane (TCNQ). Due to the limitations of available materials and technology at that time, the corresponding materials exhibited limited sensing performance for PH_3 and required operation at relatively high temperatures, often exceeding 300 °C. This poses potential safety risks, such as deflagration, when detecting high concentrations of PH_3. Therefore, the development of sensing materials capable of detecting PH_3 at low working temperature is of great significance.[16]

In the preliminary exploration, we employed density functional theory (DFT) calculations to identify materials that exhibit sensitivity to phosphine gas. It was discovered that bismuth

molybdate demonstrates remarkable responsiveness and adsorption behavior towards phosphine gas. Bismuth molybdate (Bi_2MoO_6) is a typical layered perovskite composite oxide, composed of $[Bi_2O_2]^{2+}$ layers and $[MoO_4]^{2-}$ octahedra, where the perovskite-type $[MoO_4]^{2-}$ form a shared octahedral structure. This configuration facilitates efficient electron ionization and endows the material with excellent gas sensitivity.[17] This behavior, combined with its moderate band gap (2.6 eV), enables the material to detect phosphine at room temperature with high sensitivity..[18] The stability and electronic properties of bismuth molybdate, as indicated by our simulations, make it a promising material for developing reliable and efficient phosphine sensors. Bi_2MoO_6 can form nanoparticles with various structures, such as nanosheets,[19] flower shapes,[20] walnut forms,[21] and yolk-shell structures,[22] depending on the synthesis strategy. For instance, Liu *et al.*[23] introduced 5% Ag into flower shapes Bi_2MoO_6 through a two-step solvothermal method and glucose reduction, achieving a detection limit of 50 ppb for NH_3 at room temperature. Ma *et al.*[24] synthesized Bi_2MoO_6/ZnO composites via secondary hydrothermal synthesis, demonstrating excellent sensing performance for n-butanol at 270 ºC. Zhang *et al.*[25] prepared walnut forms Bi_2MoO_6 nanospheres on a nanosheet base, successfully detecting 0.1 ppb H_2S at 133 ºC, with minimal sensitivity to humidity changes. These findings further confirm the sensing potential of Bi_2MoO_6 as a ternary gas-sensitive material. However, there are currently few studies focusing on the gas sensing performance and response mechanisms of Bi_2MoO_6 at room temperature.

Isopropanol (IPA), due to its relatively low viscosity and moderate polarity, facilitates the uniform nucleation and controlled growth of nanomaterials. It aids in stabilizing intermediate species during the synthesis process, which is crucial for achieving consistent particle size and shape. Ethylene glycol (EG), a high-boiling solvent, promotes the formation of a more viscous environment, leading to the growth of larger and more uniform crystals. As such, they are particularly well-suited for hydrothermal reactions, enabling better control over the morphology of the synthesized materials. Moreover, ethylene glycol also plays a role in regulating the crystal growth process by stabilizing certain aspects, thereby contributing to the achievement of specific morphologies.

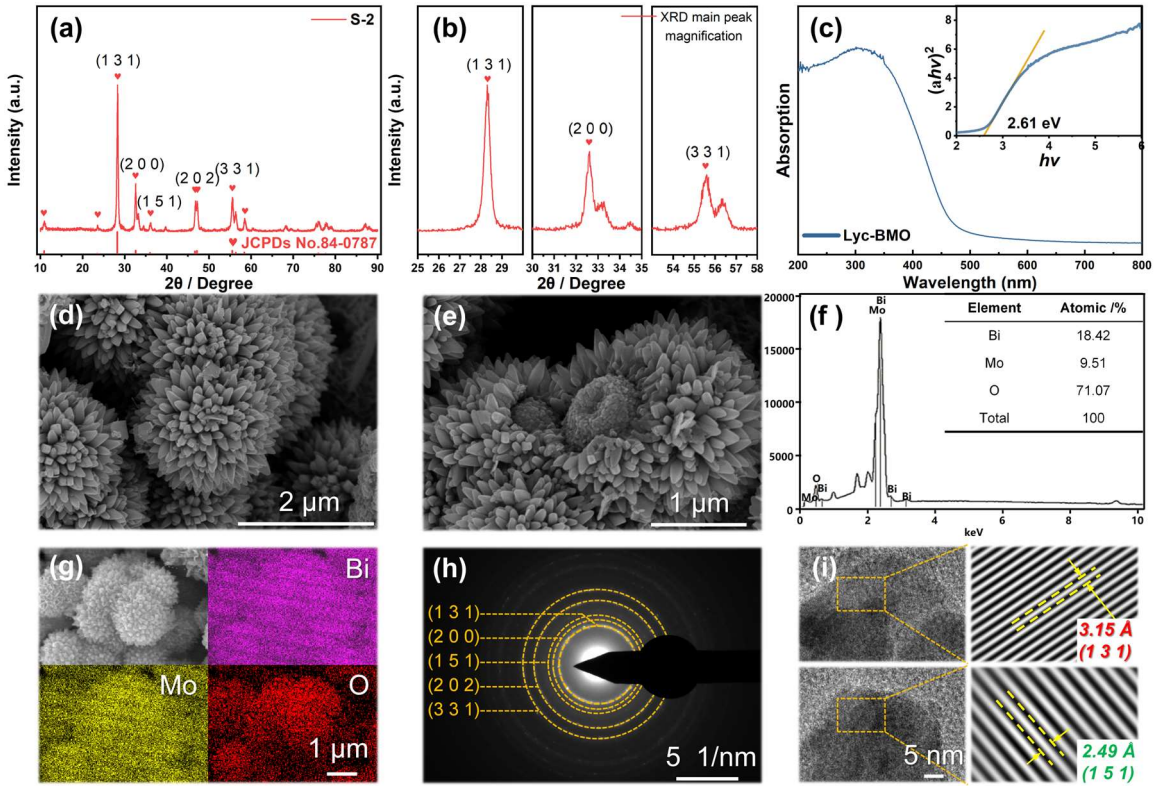

Fig. 1 | Preliminary characterization. a and **b** *XRD* pattern of S-2 and the magnified view of its main peaks. **c** *UV-Vis* absorption spectra and Tauc curve of *Lyc-Bi_2MoO_6*. **d** and **e** *SEM* images of *Lyc-Bi_2MoO_6*. **f** and **g** *EDS* and Mapping of *Lyc-Bi_2MoO_6*. **h** and **i** Selected area electron diffraction (*SAED*) pattern and *HRTEM* along with the inverse *FFT* images of *Lyc-Bi_2MoO_6*.

The lychee-like structure bismuth molybdate microspheres (*Lyc-Bi_2MoO_6*) synthesized using *IPA* and *EG* in a 3:1 ratio offers dual advantages. The outer layer of the nanoparticles, resembling a lychee shell, can ensure sufficient particle-to-particle contact while preventing the coating from becoming too dense. Inside, the particles are composed of smaller micro-particles forming the "flesh", providing abundant adsorption and reaction sites. The *PH_3* sensing performance of *Lyc-Bi_2MoO_6* at room temperature surpasses that of Bi_2MoO_6 particles with other morphologies. This paper focuses on the room-temperature *PH_3* sensing performance of *Lyc-Bi_2MoO_6* and its gas-sensing mechanism analysis.

Methods

Preparation of Lychee-like Bi_2MoO_6

Lyc-Bi_2MoO_6 was synthesized using a solvothermal approach. Initially, 1.94 g of Bismuth Nitrate Pentahydrate and 0.484 g of Sodium Molybdate Dihydrate were separately dissolved in 10 mL of *EG* while stirring magnetically. Subsequently, the two solutions were gradually

combined with 60 mL of *IPA* under continuous stirring until a homogeneous mixture was achieved. This uniform liquid was then transferred to high-pressure reactors, where it was warmed to 160 ºC-15 hours. Upon natural cooling, resultant outcomes were centrifuged thrice using deionized water and ethanol, followed by freeze-drying for 48 hours. The dried powder was then annealed at 400 ºC-2 hours. Samples were synthesized with varying ratios of *EG* to *IPA*-specifically 0:8, 2:6, 4:4, 6:2, and 8:0-designated as S-x, where x represents 1 through 5, respectively.

Preparation of Bi_2MoO_6 Sensor

Sensing electrodes were constructed by depositing a homogeneous suspension of Bi_2MoO_6 powder mixed with Deionized (*DI*) water onto electrode substrates made of Pt-integrated Al_2O_3 (purchased from Wuhan Huachuang Ruike *Co., LTD*). As shown in Figure S5, mass flow controllers (*MFCs*) were utilized to inject a standard mixed PH_3 gas, maintaining constant relative humidity (around 60%±2%) within the testing chamber. The initial PH_3 concentration, supplied by Jinan Deyang Special Gases *Co., Ltd.*, was 30.2 ± 0.6 ppm, with the balance comprising air, and total flow across the *MFCs* was 600 sccm.

Gas sensing measurement

Stable resistance (*R*) in air is denoted as R_a, while that in target gas is termed R_g. Sensor response (*S*) is calculated using the formula $S=[(R_a/R_g)-1]\times 100\%$. Response time ($\tau_{response}$) and recovery time ($\tau_{recovery}$) are defined as durations required for *S* to attain 90% of the change.

Results

Characterization discussion

XRD pattern of S-2, as shown in Figure 1a, reveals the highly crystalline nature of *Lyc-Bi_2MoO_6*, characterized by narrow and sharp peaks. Prominent diffraction peaks at $2\theta = 28.30^o$, 32.60^o, and 46.80^o correspond to the (131), (200), and (202) crystal planes of JCPDs No. 84-0787, respectively. Additionally, Figure S2 illustrates the variations in X-ray diffraction (*XRD*) patterns among all samples. When pure *IPA* was used as the solvent, S-1, identified as $Bi_{2x}Mo_{1-x}O_3$, displayed diffraction peaks in line with JCPDs No. 23-1032, where the peak intensity and broadness indicated relatively low crystallinity. In contrast, for solvent ratios of 4:4 and 6:2, the *XRD* spectra of S-3 and S-4 exhibited no impurity-related peaks, confirming the high

crystallinity of the resulting Bi_2MoO_6. Notably, when *EG* was used as the sole solvent, the *XRD* pattern of S-5 revealed strong peaks corresponding to JCPDs No. 85-1329, indicating the presence of Bi. These findings underscore the importance of using a mixed solvent of *EG* and *IPA* to achieve highly crystalline Bi_2MoO_6, especially with the 2:6 solvent ratio. Calculations based on the Debye-Scherrer formula determined the typical grain dimensions of S-x (x=1, 2, 3, 4, 5) to be 6.8 nm, 22.0 nm, 17.6 nm, 16.6 nm, and 10.1 nm, respectively. This indicates that *Lyc-Bi_2MoO_6* possesses the largest grain size, with notable fluctuations in grain size observed over distinct crystal planes. Figure 1c presents the UV absorption spectrum of *Lyc-Bi_2MoO_6*, obtained using a UV-visible spectrometer. The absorption begins around 350 nm, with a significant decline in the ultraviolet region. The inset illustrates the optical bandgap properties of *Lyc-Bi_2MoO_6*, estimated using the Tauc method ($(\alpha hv)^2=K(hv-E_g)$). The calculated bandgap for *Lyc-Bi_2MoO_6* is approximately 2.61 eV, indicating its suitability as a semiconductor material for gas sensing applications.[26] The absorption spectra of other samples can be viewed in Figure S1. Overall, the bandgap width decreases with the increasing amount of *EG*, and a notable shift occurs when *EG* is used as the solvent. Based on the trend of the band gap values of different bismuth molybdate samples (Fig. S1e) and the corresponding phosphine sensing performance trends (Fig. 5e), the significant response of *Lyc-Bi_2MoO_6* at room temperature to low concentrations of phosphine is considered to be associated with its moderate band gap value. Figure S3 displays the FT-IR absorbance spectra of samples S-1 to S-5. The results demonstrate that FT-IR analysis is indeed valuable for investigating the functional groups and bonding interactions within the materials, offering deeper insights into their sensing mechanisms. In the 1000-800 cm^{-1} range, Mo=O stretching vibration peaks can be observed. The absorption peak of the S-2 sample is slightly sharper or stronger, indicating a potentially higher concentration of Mo=O double bonds or an optimized surface electronic distribution. In the 800-600 cm^{-1} range, Bi-O and Mo-O-Mo bridging vibration peaks are observed, with some differences in peak shape across the samples. The S-2 sample shows relatively stronger and clearer absorption signals in this region, suggesting that the Bi-O and Mo-O-Mo structures in S-2 may be more stable or present in higher content. This structural optimization could enhance the sample's surface catalytic activity, promoting the adsorption and oxidation of phosphine molecules.

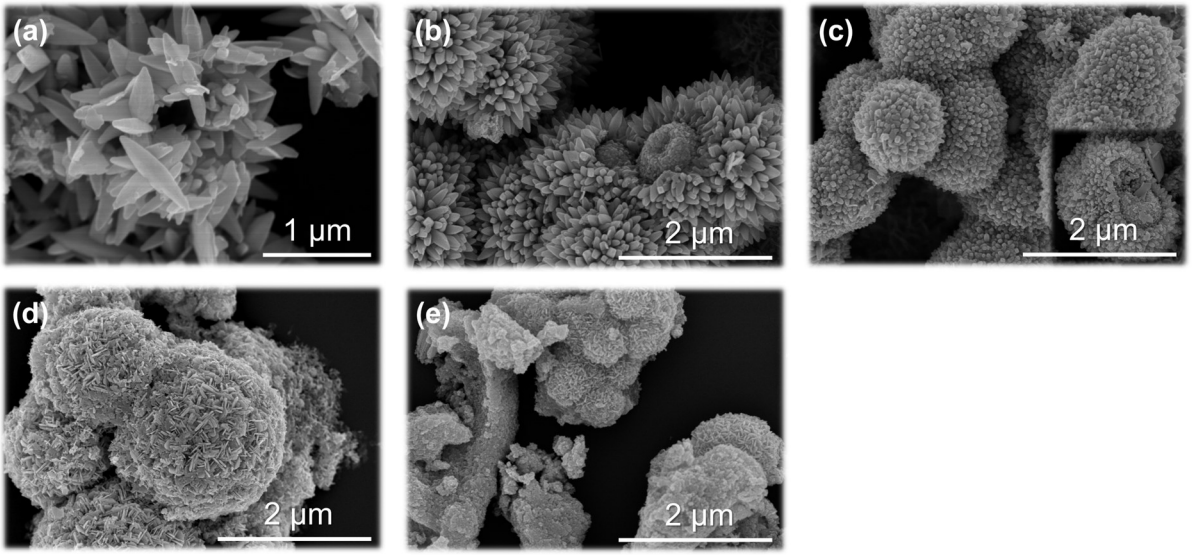

Fig. 2 | *SEM* images of Bi_2MoO_6 synthesized from different solvent ratios (EG : IPA). a 0:8, **b** 2:6, **c** 4:4, **d** 6:2, **e** 8:0.

From the *SEM* images (Figs. 1d and 1e), the lychee-shell-like Bi_2MoO_6 described in this work can be clearly observed, with particles approximately 2 μm in diameter. It can be roughly divided into an inner layer (the "flesh" composed of nanoparticles) and an outer layer (the lychee shell with a thickness around 400 nm). The outer layer of the lychee-shell structure ensures sufficient particle-to-particle contact while preventing the coating from becoming overly dense. This creates, on a macroscopic level, favorable channels for the penetration and diffusion of target gas molecules, thereby shortening the response process. Meanwhile, the "flesh" forming the inner layer provides abundant active sites for gas-sensing reactions, enhancing electron transfer between the gas and the sensing material at a microscopic level.[27] From the quantitative *EDS* results (Figure 1f), it is evident that the sample contains approximately 18.42% Bi and 9.51% Mo in terms of atomic percentage. The *EDS* mapping image in Figure 1g further confirms that Bi and Mo are uniformly distributed throughout the sample. The selected area electron diffraction (SAED) pattern of *Lyc-Bi_2MoO_6* shown in Figure 1h, captured by *HRTEM*, along with the inverse *FFT* images (Figure 1i) obtained by Digital Micrograph, both reveal diffraction rings and lattice fringe spacings corresponding to the (131), (200), (151), (202), and (331) planes in JCPDs No.84-0787, identified that (131) serves as the primary exposed facet of Lyc-Bi_2MoO_6.[28,29]

The *SEM* images of Bi_2MoO_6 synthesized from different solvent ratios (Figure 2a-e and

Figure S10) provide insights into the formation mechanism of *Lyc-Bi_2MoO_6*. When *IPA* is used as the sole solvent, uniformly smooth crystalline nanoparticles are observed. Upon the addition of a small amount of *EG*, these crystalline nanoparticles assemble into nanospheres, suggesting that *EG* serves as the primary growth complexing agent for the spherical structure. When the *EG* to *IPA* ratio is 2:6 and 4:4, the lychee-like Bi_2MoO_6 structure, as described, is observed. However, with a further increase of *EG*, the lychee shell-like structure disappears, transforming into nanospheres composed of sheet-like particles, indicating that sufficient *IPA* is required as the driving force for the growth of crystalline particles. The structure obtained with a solvent ratio of 4:4 better aligns with the lychee-like structure we refer to, yet its *PH_3* sensing performance at room temperature is inferior to that of *Lyc-Bi_2MoO_6* obtained with a solvent ratio of 2:6 during gas sensitivity testing. However, when *EG* is used as the sole solvent, the *SEM* images reveal a morphology with a considerable amount of dispersed structures. This phenomenon may be related to the Bi precipitation behavior observed in the *XRD* analysis. Figs. 3a-3e displays the N_2 adsorption/desorption isotherms, pore size distribution, and specific surface area (*SSA*) of all synthesized Bi_2MoO_6 samples. The IV-type isotherms with H3 hysteresis loops observed in the Bi_2MoO_6 samples indicate a pronounced mesoporous structure, which is further confirmed by the average pore size analysis (Figure 3f). In comparison, the Lyc structure's specific surface area is not the highest, being lower than that of S-5. This suggests that while *Lyc-Bi_2MoO_6* can enhance gas sensitivity through more active sites, it is not the sole factor influencing its performance.

Additionally, the chemical forms and oxygen varieties of *Lyc-Bi_2MoO_6* were identified by *XPS*, with the resulting spectra shown in Figure 4a. The documented spectra confirm the presence of Bi, Mo, and O in *Lyc-Bi_2MoO_6*. Figure 4b illustrates that the two main peaks of the Bi 4f orbitals appear around 158.97 eV and 164.30 eV, corresponding to the binding energies of Bi $4f_{7/2}$ and Bi $4f_{5/2}$, respectively.[30,31] The spin-orbit splitting of 5.33 eV indicates that Bi is in the +3-oxidation state. The Mo 3d orbitals (Figure 4c) exhibit two main peaks, Mo $3d_{5/2}$ and Mo $3d_{3/2}$, located at approximately 232.24 eV and 235.47 eV, indicating that Mo is in the +6-oxidation state, consistent with Bi_2MoO_6.[32,33] It can also similarly be evidenced by the Mo $3p_{3/2}$

and Mo $3p_{1/2}$ peaks located at 398.16 eV and 415.69 eV in Figure 4d. Furthermore, Figure 4e displays the high-resolution O1s spectrum, with two sub-peaks at 529.95 eV and 530.82 eV. The primary peak corresponds to lattice oxygen, associated with Mo-O and Bi-O bonds, while the higher binding energy sub-peak at 532.83 eV is attributed to surface-adsorbed oxygen species.[34,35] The percentages assigned to Mo-O bond and Bi-O bond are 27.2% and 60.4%, respectively. The *XPS* spectra for other samples (Figure S4) are included in the "Supporting Information".

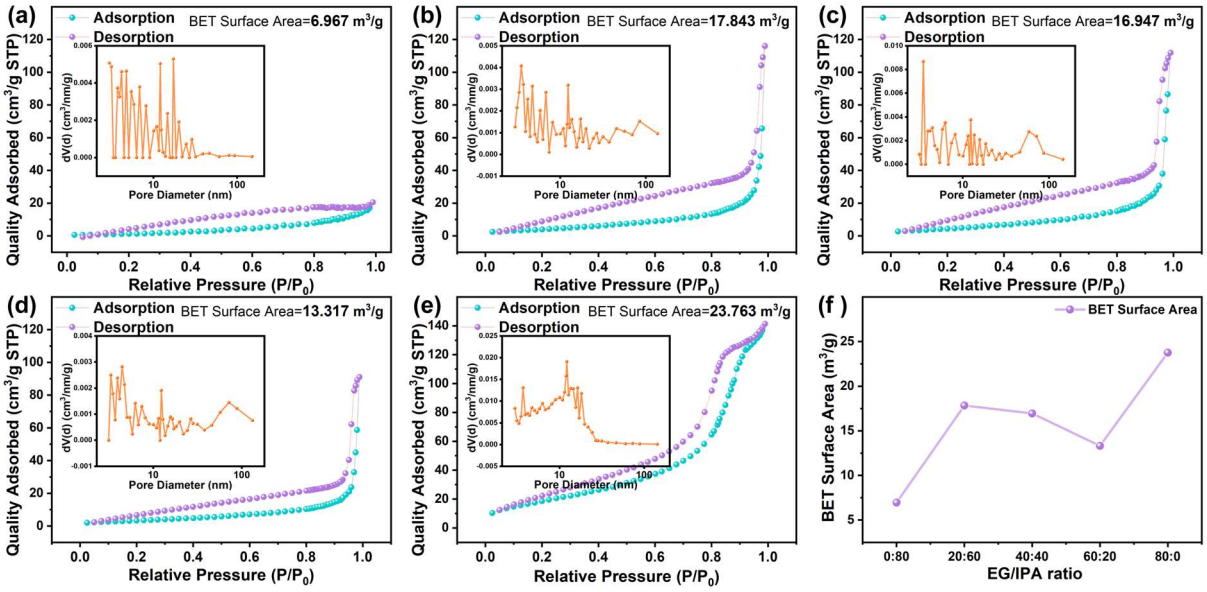

Fig. 3 | The nitrogen adsorption-desorption isotherm and pore size distribution curve (insert graph). **a-e** Nitrogen adsorption-desorption results of S-1 to S-5, **f** *BET* surface areas comparison.

It is noteworthy that there are significant variations in the elemental peak intensities across the *XPS* full spectra of the samples, particularly in sample S-5, where the Bi 4f peak is markedly diminished due to potential Bi precipitation. In sample S-1, the peak area analysis of Bi and Mo indicates a Bi to Mo ratio of 3:1, resulting in a surface composition of $Bi_{1.2}Mo_{0.4}O_3$. Another distinction in the *XPS* survey spectrum is the O 1s peak, where samples S-2, S-3, and S-4 exhibit a pronounced peak near 533 eV, attributed to adsorbed oxygen. Moreover, the binding energy corresponding to adsorbed oxygen in S-2 is 1.5 eV lower than that in S-3 and S-4. This lower binding energy facilitates the adsorption of oxygen molecules on the material's surface at room temperature, which contributes to the enhancement of the sensing performance. The supplementary information shows the thermogravimetric analysis (TGA) of sample S-2.

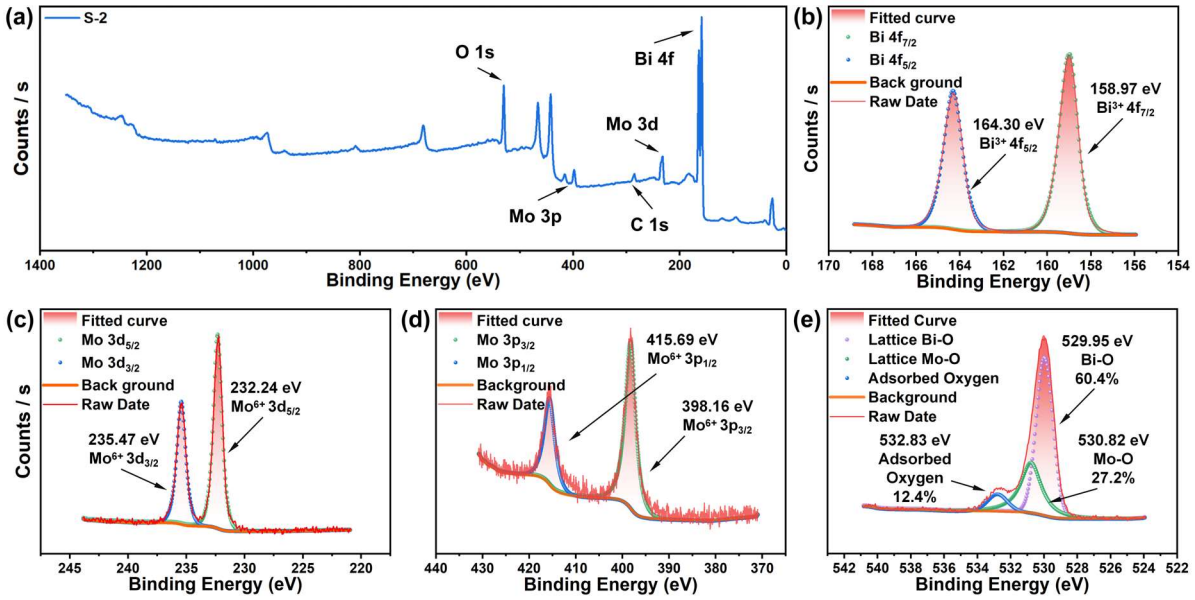

Fig. 4 | *XPS* analysis of *Lyc-Bi_2MoO_6*. **a** Survey spectrum. **b** Bi 4f spectra. **c** and **d** Mo 3d and 3p spectra. **e** O 1s spectra.

Gas sensing performance

This section presents a detailed analysis of *Lyc-Bi_2MoO_6*'s phosphine sensing performance at low concentrations under room temperature (25±0.2 °C). All tests were conducted in controlled conditions with 60±0.5 % relative humidity. Figure 5a compares the response of Bi_2MoO_6 synthesized with different solvent ratios to 1 ppm PH_3, where *Lyc-Bi_2MoO_6* synthesized at a 2:6 ratio of *EG* to *IPA* stood out. *XRD* results reveal that particles synthesized with pure *EG* not only exhibit notable Bi precipitation but also display irregular morphology and size. This confirms that using *IPA* and *EG* as solvents is an effective and appropriate strategy for developing PH_3 sensing materials at room temperature. Figure 5b presents the continuous response (*S*) of three sensors coated with *Lyc-Bi_2MoO_6* films to PH_3 concentrations of 0.15, 0.3, 0.6, 1.2, 2.25, and 4.5 ppm.[36,37] The variations in response to different PH_3 concentrations are clearly visible, and there is excellent consistency among the three sensors. The linear fitting results in Figure 5c demonstrate that *Lyc-Bi_2MoO_6* exhibits a highly linear response to low concentrations of PH_3, with R^2 = 0.9992. Figure S9c illustrates the linear relationship between response and concentration over a broader concentration range. The results indicate that within this extended range (0.15-30 ppm), the sensor not only maintains a strong linear correlation but also exhibits minimal variation compared to the smaller

concentration range (0.15-4.5 ppm). This characteristic facilitates the calibration of the sensing material during practical applications. The magnified response graph (Figure 5d) shows the response ($\tau_{response}$) and recovery ($\tau_{recovery}$) times of *Lyc-Bi_2MoO_6* to 0.6 ppm *PH_3*, where the sensor begins reacting within 3 seconds of exposure and completes its response in approximately one minute ($\tau_{response}$ generally decreases as gas concentration increases).

The lowest measured *PH_3* concentration in the test was 150 ppb, while the theoretical detection limit of (LOD) *Lyc-Bi_2MoO_6* for *PH_3* was calculated by LOD = ($3\times\Gamma_y/\Gamma$) to be less than 100 ppb.[38] Here, Γ_y is the standard deviation of the response (which is the variability or noise level of the measurement obtained by testing 80 points with target gas) and Γ is the slope of the linear fitting equation. The detailed calculation results are included in "Supporting Information". Selectivity to the target gas is crucial for practical applications.[39] Figure 5e illustrates the sensitivity of *Lyc-Bi_2MoO_6* at room temperature to potential interfering gases at specific concentrations, such as ammonia, hydrogen sulfide, carbon dioxide, carbon monoxide, ethylene. Figure S8 presents the dynamic response curves of the Lyc-Bi_2MoO_6 sensor to NH_3, H_2S, CO_2, CO and C_2H_4 gases. To mitigate this problem, we plan to explore the use of sensor arrays, where multiple sensors with different material compositions or operating conditions could work together. This system could effectively differentiate between phosphine and other gases by analyzing the combined responses from the array, thereby improving the overall selectivity. Hence, by considering these sensor readings, we can mitigate the cross-sensitivity of *Lyc-Bi_2MoO_6*. Therefore, *Lyc-Bi_2MoO_6* is considered to exhibit excellent *PH_3* sensing performance under specific environmental conditions. Additionally, *Lyc-Bi_2MoO_6*'s responses to 0.3 and 0.6 ppm *PH_3* were evaluated across several cycles to ensure reproducibility. Figure 5f shows that *S* of *Lyc-Bi_2MoO_6* to these concentrations remain stable over a minimum of 10 continuous cycles, with a deviation less than 10% and an average deviation under 5%. Figure 5f also shows the results of 1.2 ppm *PH_3* response assessments carried out per week across the same collection of *Lyc-Bi_2MoO_6* sensors. Even after several weeks, *Lyc-Bi_2MoO_6* maintained a certain level of sensitivity to *PH_3*, with the maximum response attenuation being 9.46% over 10 weeks. Notably, after 7 weeks, the rate of attenuation began to stabilize. Figure S7 presents the humidity testing results, indicating that within the 60% relative humidity range (45%-70%), minor fluctuations in humidity introduce an error of no more than ±2% in the PH_3 response measurements. Moreover, Table 1 compares the gas detection capabilities of *Lyc-Bi_2MoO_6* with other *PH_3* sensing materials, highlighting parameters including sensitivity, operating

temperature, and $\tau_{response}$. Previous studies clearly show that *PH₃* sensors based on Fe_2O_3, $CaFeO_{2.5}$, SnO_2-ZnO, and SnO_2-ZrO_2 require higher operating temperatures to achieve optimal sensing performance. Among these, SnO_2-based composite sensors exhibit good sensing performance for ppm-level *PH₃*, including high responsiveness and sensitivity. All the experimental results indicate that even at room temperature and lower *PH₃* concentrations, *Lyc-Bi_2MoO_6* provides significant gas sensitivity. Therefore, *Lyc-Bi_2MoO_6* is considered a promising high-sensitivity *PH₃* sensing material for room-temperature applications.

Figure S9 shows the continuous tracking response curves of the *Lyc-Bi_2MoO_6* sensor to phosphine concentrations ranging from 10 to 30 ppm, as well as cyclic response curves for larger concentration differences. From these curves, it can be seen that the theoretical upper detection limit of *Lyc-Bi_2MoO_6* for phosphine gas at room temperature exceeds 30 ppm, and the sensor is able to return to its initial state after each response.

Table 1

Comparison of different metal oxide-based phosphine sensors.

Materials	Operating *Temp*/°C	Concentration/ppm (Response)	Formulas	$\tau_{response}$	*REF*
Fe_2O_3	360	100 (29.4)	$S=R_a/R_g$	1 hour	[40]
$CaFeO_{2.5}$	360	5 (3.5)		15 min	[13]
SnO_2-ZnO	310	0.4 (2.4)	$S=(R_a-R_g)/R_g$	1 min	[12]
SnO_2-ZrO_2	350	0.1 (260)		1 min	[14]
Modified porous Si	RT	1 (1.19)	$S=R_a/R_g$	4 min	[41,42]
Lyc-Bi_2MoO_6	RT	0.6 (25 %)	$S=(R_a-R_g)/R_g\times100\%$	65 sec	This work

* RT represents room temperature.

Gas-sensing mechanism

Density functional theory calculations are increasingly employed to explore gas-sensing mechanisms. In this study, we conducted *DFT* calculations to investigate the phosphine sensing mechanism of *Lyc-Bi_2MoO_6*. A thorough analysis was performed on the geometrical structure, adsorption energy, orbital hybridization, and electron transfer of the adsorption system. The sensor's response and recovery capabilities were also evaluated. The results of this research may assist in validating and promoting the exploration of *Lyc-Bi_2MoO_6* for potential applications in *PH₃* gas sensors. Relevant computational parameters can be referenced in the methods below. Figures 6a and 6b display the band structure and DOS of the Bi_2MoO_6 supercell, demonstrating that Bi_2MoO_6 is an indirect bandgap semiconductor with a bandgap width of 2.579 eV, nearly

matching the observed value of 2.61 eV. The O 2p orbitals occupy the upper edge of the valence band in the total density of states (*TDOS*), while hybridized p orbitals with Mo 4d fill the high-energy regions of the valence band. The Bi 6s orbitals contribute minimally near the Fermi level, and the conduction band is primarily composed of hybridized Bi 6p and Mo 4d orbitals. During PH_3 adsorption, electrons transition from the hybridized orbitals to the Bi 6p orbitals. The (131) plane was chosen for PH_3 adsorption studies due to its relatively stable surface energy.[43] Table 2 lists the adsorption energy (E_{ads}), adsorption distances, and charge transfer (Q_t) for adsorption configurations α, β, and γ. On the surface, PH_3 tends to adsorb at the top Bi site, as shown in the adsorption model α in Figure 6c.

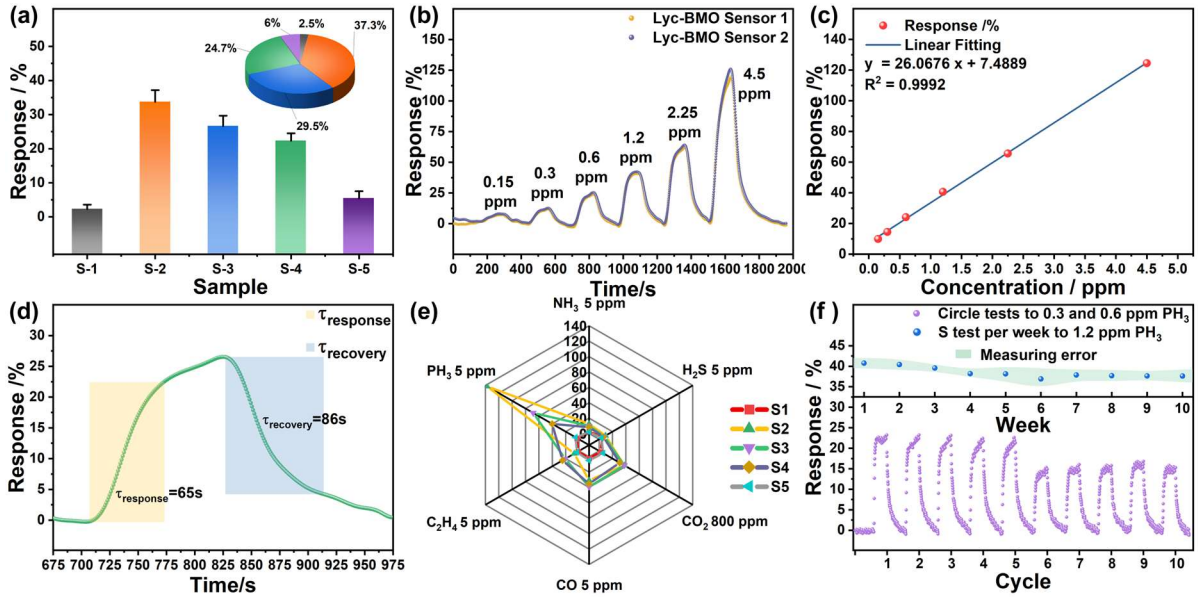

Fig. 5 | Trace-gas sensing measurement. a Response of Sample S-1to S-5 to 1 ppm PH_3. **b** Response schematic diagram of *Lyc-*Bi_2MoO_6 to PH_3 concentration changes. **c** Linear relationship of response and concentration. **d** Magnified response of *Lyc-*Bi_2MoO_6 to 0.6 ppm PH_3. **e** Sensitivity of *Lyc-*Bi_2MoO_6 at room temperature to potential interfering gases. **f** Schematic diagram of a cyclic test and per week response with error distribution.

Table 2

The adsorption performance of PH_3 on Bi_2MoO_6 (131).

Adsorption model	E_{ads} * /eV	Distance/Å	Q_t /e
α	0.385	3.062	0.02
β	1.220	3.739	-0.01
γ	1.909	3.978	-0.09

* Equation 3 for E_{ads} is provided in methods.[44]

Figs. 6c-6e illustrate the electron density difference (*EDD*) maps of PH_3 adsorption on the

surface sites of Bi, Mo, and O on Bi_2MoO_6 (131), denoted as models α, β, and γ, respectively. In these maps, blue represents electron loss, and red represents electron gain.[45] According to Table 2, only in configuration does PH_3 transfer electrons to the surface. Figs. 6f-6h show *EDD* slice views for adsorption configurations α, β and γ, along with the electron loss and gain in the slice perpendicular to the Z-axis.[46,47] It can be observed that in the Bi top-site adsorption (model α), PH_3 transfers the most charge to the surface, with electrons more concentrated within the bulk. In contrast, for the Mo and O top-site adsorptions (models β and γ), electrons accumulate between the surface and the adsorbed PH_3 molecules, and PH_3 captures a certain number of electrons. All models have positive E_{ads} values, indicating that PH_3 adsorption is a physical adsorption process requiring endothermic energy input. Positive adsorption energy usually indicates that the adsorption process is endothermic, which is less common in gas-solid interactions as they are generally exothermic. A positive value suggests that the interaction between the gas molecules and the surface is weaker than expected and that energy is required to adsorb the gas onto the surface. Notably, adsorption model α exhibits relatively stable adsorption, while configurations β and γ are unstable and sensitive to external conditions such as temperature and humidity.

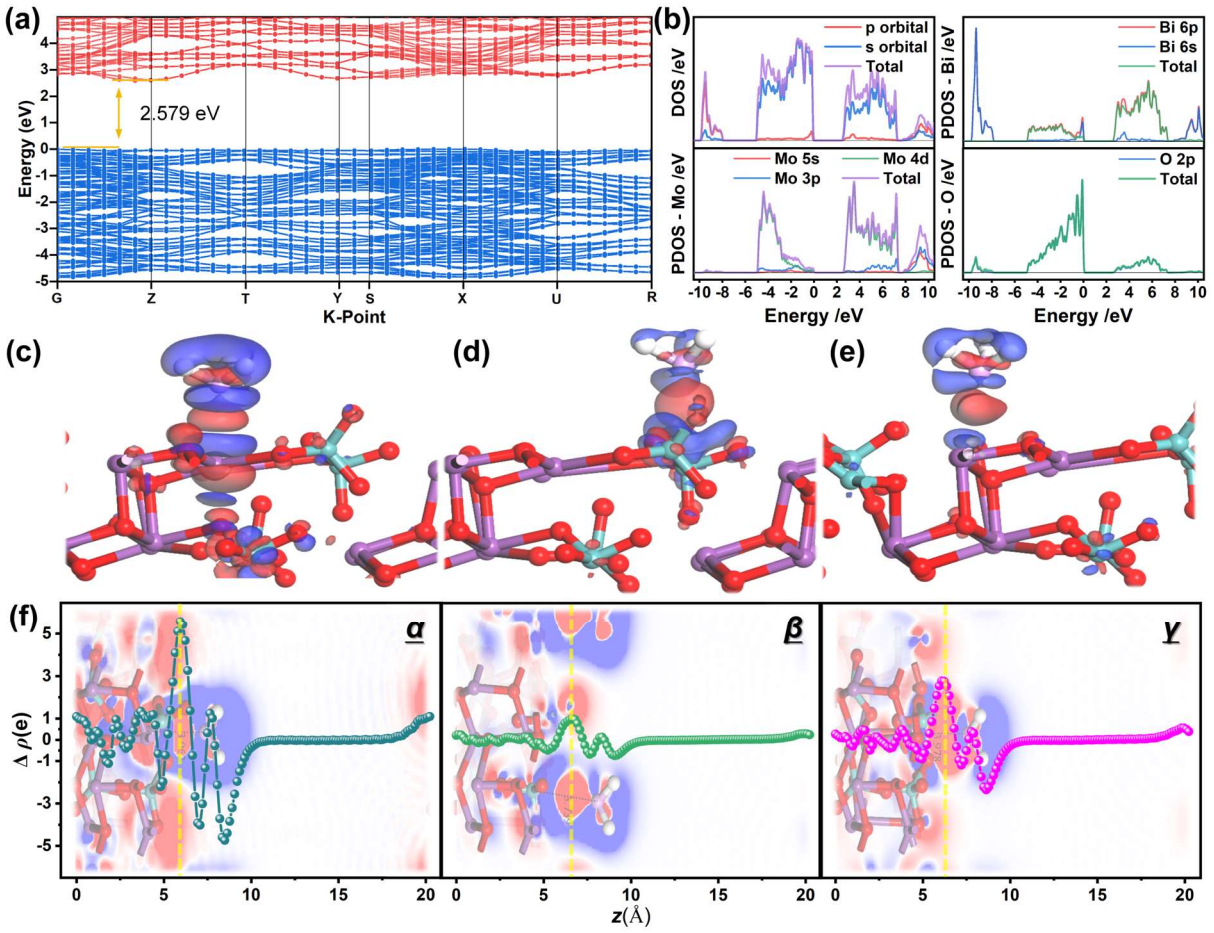

Fig. 6 | Adsorption behavior of *PH_3* under density functional theory. a The band structure of Bi_2MoO_6. **b** Partial Density of States of Bi_2MoO_6. Optimal model and EDD distribution of *PH_3* adsorption models on Bi top **c**, Mo top **d** and O top **e**. **f** *EDD* slice views for adsorption configurations α, β and γ, along with the electron loss and gain in the slice perpendicular to the Z-axis.

Figure 7a presents a schematic diagram of the room temperature sensing mechanism of *Lyc-Bi_2MoO_6* for *PH_3*. During O_2 adsorption, electrons are captured from the surface, while *PH_3* donates electrons to the surface and reduces adsorbed oxygen to free O_2. In brief, at room temperature, the surface-adsorbed O_2 captures free electrons from the conduction band of *Lyc-Bi_2MoO_6*, converting them into O_2^- ions (R1), which leads to an increase in the potential barrier and the expansion of the electron depletion region.[48,49] Upon exposure to the reducing *PH_3* gas, it is adsorbed onto the surface in the form of *PH_3 (ads)* (Equation 1, R2). During the R3 process, a portion of the surface O_2^- is reduced to O_2, and electrons are transferred back to the *Lyc-Bi_2MoO_6* substrate (Equation 2). At this stage, the electrons previously captured by O_2^- are returned to Bi_2MoO_6, reducing the barrier height and the thickness of the depletion layer, significantly lowering the sensor's resistance. Eventually, when the *PH_3* concentration becomes

stable, electron transfer reaches equilibrium (R4), and the sensor's response stabilizes (Figure 7b). Figure 7c explains the adsorption behavior through the space charge layer model, showing that after PH_3 adsorption, due to electron transfer to the surface, the bandgap of *Lyc-*Bi_2MoO_6 is reduced to 1.283 eV (which is a theoretical band gap value calculated from DFT). We conducted phosphine gas-phase sensing tests in a nitrogen environment, with results shown in Figure S6. In Figure S6 a, the stable baseline resistance indicates that the baseline resistance in a nitrogen environment remains consistent over an extended period and is lower than in air. This reduction is attributed to the absence of adsorbed oxygen capturing electrons from the sensing material, which typically increases resistance. Upon introducing phosphine gas-phase analytes (Figures S6 b and c), the sensor demonstrated a sensitive response. Compared to air, the sensor's response in a nitrogen atmosphere to the same phosphine concentration was significantly reduced, registering only about 20% of the response observed in air. This indicates that the room-temperature phosphine sensing response of *Lyc-*Bi_2MoO_6 is composed of two components: electron transfer associated with desorption of adsorbed oxygen and physical adsorption of phosphine. The room-temperature resistivity and conductivity of Lyc-Bi_2MoO_6 are presented in Figure S12, with the resistivity stabilizing around 155 MΩ·cm. This provides valuable insight into the potential applications of the material in gas sensing. Electrochemical impedance spectroscopy (EIS) was conducted using a standard Randle circuit, with the equivalent circuit model illustrated in Figure S13. Charge transfer resistance (R_{ct}), interfacial capacitance (C_{dl}), and ion diffusion impedance, were analyzed to elucidate the gas adsorption-desorption process, transport mechanism, and charge accumulation effect. The results exhibit a typical Nyquist structure, where the semicircle in the low-frequency region indicates a faster interfacial charge transfer, which is beneficial for gas sensing response. The linear segment in the high-frequency region is typically associated with Warburg impedance (W), reflecting diffusion-controlled processes such as electron or ion transport. The angle of the linear region approaches 45°, indicating low internal diffusion resistance within the material. This suggests enhanced electron and ion diffusion, leading to a higher charge transfer rate, which may explain the rapid response of Lyc-Bi_2MoO_6 to phosphine gas at room temperature.

Lyc-Bi₂MoO₆ demonstrates excellent sensing performance for detecting low concentrations of phosphine at room temperature, providing a valuable reference for the development of semiconductor-based *PH₃* sensing materials.

$$PH_3\,(g) \rightarrow PH_3\,(ad) \quad (1)$$

$$PH_3\,(ad) + O_2^- \leftrightarrow PH_3^{x+} + O_2\,(ad) + (x+1)\,e^- \quad (2)$$

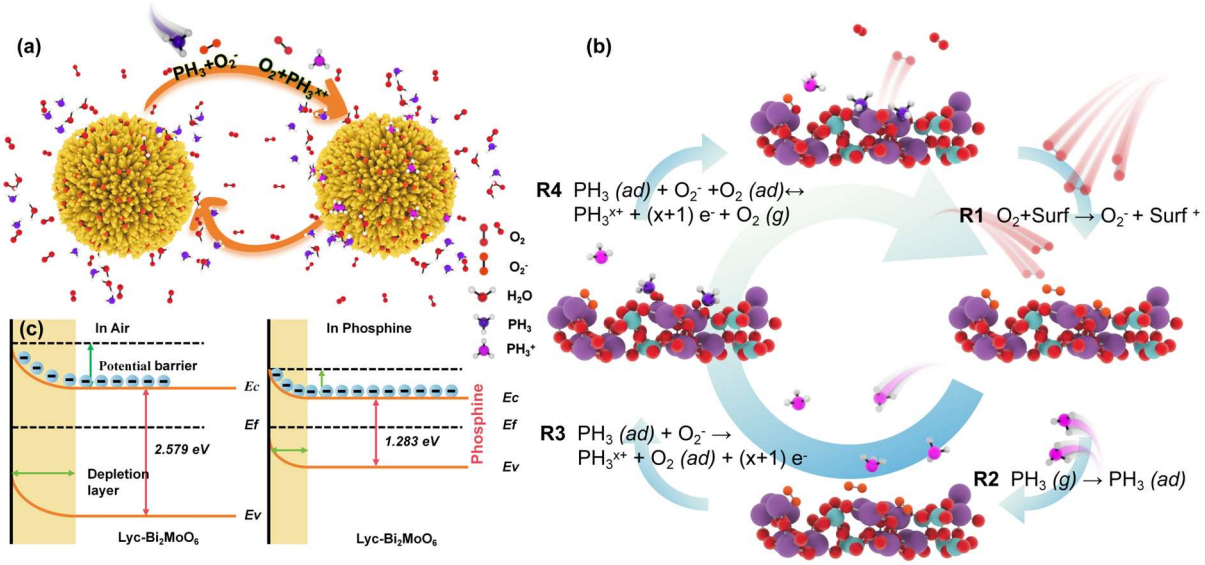

Fig. 7| Schematic diagram of response process. a and **b** Gas-sensing process schematic, **c** Band diagram of *PH₃* before and after adsorption upon *Lyc-Bi₂MoO₆*.

Discussion

This study presents a gas sensor based on *Lyc-Bi₂MoO₆* synthesized via a solvothermal process, designed for detecting *PH₃* at ppb level. The sensor's performance in detecting *PH₃* at room temperature was investigated from multiple perspectives, including real-time response to varying *PH₃* concentrations, cyclic response, and long-term stability testing. The sensor can initiate action within 3 s of exposure to *PH₃* and completes the response around 60 seconds, achieving a practical LOD around 150 ppb, which is below the OSHA permissible exposure limit. Characterization results indicate that the performance of the *Lyc-Bi₂MoO₆* sensor towards *PH₃* is attributable to its lychee-like nanostructure. The outer "lychee shell" ensures sufficient contact between particles while maintaining a non-dense coating, while the internally smaller "flesh" particles provide more effective adsorption and reactive sites. The narrow bandgap and rapid mobility of charge carriers further contribute to its sensitivity. Despite the promising low-concentration detection capability of the *Lyc-Bi₂MoO₆* at room temperature, further

investigation into the mechanisms and theoretical analysis is needed to enhance *Lyc-Bi_2MoO_6*-based *PH_3* sensing materials, which may advance the application of semiconductor gas sensors in *PH_3* detection.

AUTHOR INFORMATION

Corresponding Authors

Chao Zhang - College of Mechanical Engineering (Dean), Yangzhou University, Yangzhou 225127, Jiangsu Province, P.R. China; orcid.org/0000-0003-2346-6770; Email: zhangc@yzu.edu.cn.

Authors

Xiaoxi He - College of Mechanical Engineering, Yangzhou University, Yangzhou 225127, Jiangsu Province, P.R. China; Department of Applied Science and Technology (DISAT), Politecnico di Torino, Corso Duca Degli Abruzzi 24, Torino 10129, Italy; orcid.org/0009-0005-2733-9383; Email: DX120230095@stu.yzu.edu.cn.

Jinyong Xu - College of Mechanical Engineering, Yangzhou University, Yangzhou 225127, Jiangsu Province, P.R. China; Email: jinyong_xu2021@126.com.

Jean-Marc Tulliani - Department of Applied Science and Technology (DISAT), Politecnico di Torino, Corso Duca Degli Abruzzi 24, Torino 10129, Italy; Email: jeanmarc.tulliani@polito.it.

Yixiang Bian - College of Mechanical Engineering, Yangzhou University, Yangzhou 225127, Jiangsu Province, P.R. China; Email: yxbian@yzu.edu.cn.

Notes

The authors declare no competing financial interest.

Data Availability Statement

Authors can confirm that all relevant data are included in the paper and/or its supporting information files. Additional data are available from the corresponding author upon reasonable request.

ACKNOWLEDGMENTS

This work was supported by the Outstanding Youth Foundation of Jiangsu Province of China under Grant No. BK20211548; the Yangzhou Science and Technology Plan Project (No. YZ2023246) and Postgraduate Research and Practice Innovation Program of Jiangsu Province of China (No. KYCX24_3734).

Supporting Information

Supporting Information is available from the author. Additional experimental, schematic and illustration of experimental sensor testing setup (Figures S1-S13), and partial experimental details can be found in it.

References

(1) Feng, W.; Zhou, Q.; Wang, L.; Ju, W.; Yang, Y. Influence of Defect and Doping on the Sensitivity and Adsorption Capacity of Zr_2CO_2 toward PH_3 Gas. *Comput. Mater. Sci.* **2024**, *244*, 113263. https://doi.org/10.1016/j.commatsci.2024.113263.

(2) Jagadeesan, R.; Singarayan, V. T.; Chandra, K.; Ebert, P. R.; Nayak, M. K. Potential of Co-Fumigation with Phosphine (PH_3) and Sulfuryl Fluoride (SO_2F_2) for the Management of Strongly Phosphine-Resistant Insect Pests of Stored Grain. *J. Econ. Entomol.* **2018**, *111* (6), 2956-2965. https://doi.org/10.1093/jee/toy269.

(3) Nath, N. S.; Bhattacharya, I.; Tuck, A. G.; Schlipalius, D. I.; Ebert, P. R. Mechanisms of Phosphine Toxicity. *J. Toxicol.* **2011**, *2011*, 1-9. https://doi.org/10.1155/2011/494168.

(4) Feng, J.; Ma, L.; Wang, C.; Ma, Y.; Sun, X.; Jia, L.; Ning, P.; Zhang, R.; Wang, F.; Li, K. Catalytic Decomposition Mechanism of PH_3 on 3DCuO/C and High Value Utilization of Deactivated Catalysts. *Small* **2023**, *19* (28), 2301169. https://doi.org/10.1002/smll.202301169.

(5) Agrafioti, P.; Kaloudis, E.; Bantas, S.; Sotiroudas, V.; Athanassiou, C. G. Phosphine Distribution and Insect Mortality in Commercial Metal Shipping Containers Using Wireless Sensors and CFD Modeling. *Comput. Electron. Agric.* **2021**, *184*, 106087. https://doi.org/10.1016/j.compag.2021.106087.

(6) Brabec, D.; Morrison, W.; Campbell, J.; Arthur, F.; Bruce, A.; Yeater, K. Evaluation of Dosimeter Tubes for Monitoring Phosphine Fumigations. *J. Stored Prod. Res.* **2021**, *91*, 101762. https://doi.org/10.1016/j.jspr.2021.101762.

(7) Agrafioti, P.; Kaloudis, E.; Bantas, S.; Sotiroudas, V.; Athanassiou, C. G. Modeling the Distribution of Phosphine and Insect Mortality in Cylindrical Grain Silos with Computational Fluid Dynamics: Validation with Field Trials. *Comput. Electron. Agric.* **2020**, *173*, 105383. https://doi.org/10.1016/j.compag.2020.105383.

(8) Agrafioti, P.; Sotiroudas, V.; Kaloudis, E.; Bantas, S.; Athanassiou, C. G. Real Time Monitoring of Phosphine and Insect Mortality in Different Storage Facilities. *J. Stored Prod. Res.* **2020**, *89*, 101726. https://doi.org/10.1016/j.jspr.2020.101726.

(9) Duan, G.; Huang, S.; Feng, Z.; Xie, P.; Zhang, F.; Zhou, Y.; Han, S. Three-Terminal Artificial Olfactory Sensors Based on Emerging Materials: Mechanism and Application. *Adv. Funct. Mater.* **2023**, *33* (10), 202209969. https://doi.org/10.1002/adfm.202209969.

(10) Jo, Y. K.; Jeong, S.-Y.; Moon, Y. K.; Jo, Y.-M.; Yoon, J.-W.; Lee, J.-H. Exclusive and Ultrasensitive Detection of Formaldehyde at Room Temperature Using a Flexible and Monolithic Chemiresistive Sensor. *Nat. Commun.* **2021**, *12* (1), 4955. https://doi.org/10.1038/s41467-021-25290-3.

(11) Zhang, H.; Zhang, Z.; Li, Z.; Han, H.; Song, W.; Yi, J. A Chemiresistive-Potentiometric

Multivariate Sensor for Discriminative Gas Detection. *Nat. Commun.* **2023**, *14* (1), 3495. https://doi.org/10.1038/s41467-023-39213-x.
(12) Varfolomeev, A. E.; Volkov, A. I.; Eryshkin, A. V.; Malyshev, V. V.; Rasumov, A. S.; Yakimov, S. S. Detection of Phosphine and Arsine in Air by Sensors Based on SnO_2 and ZnO. *Sens. Actuators B Chem.* **1992**, *7* (1-3), 727-729. https://doi.org/10.1016/0925-4005(92)80393-C.
(13) Eguchi, K.; Kayser, P.; Menil, F.; Lucat, C.; Aucouturier, J. L.; Portier, J. Detection of Phosphine at the Ppm Level by $Sr_{1-y}Ca_yFeO_{3-x}$ Thick Layers Pretreated with Highly Concentrated Phosphine in Air. Evidence of a Transition of the Surface Conductivity from p- to n-Type. *Sens. Actuators B Chem.* **1990**, *2* (3), 193-197. https://doi.org/10.1016/0925-4005(90)85004-I.
(14) Ratcheva, T.; Stambolova, I.; Konstantinov, K. PH3 Detection by SnO_2-ZrO_2 Thin Films. *Sens. Actuators B Chem.* **1994**, *21* (3), 199-204. https://doi.org/10.1016/0925-4005(94)01246-6.
(15) Perez, H.; Clemendot, S.; Derost, G.; Ruaudel-Teixier, A.; Barraud, A.; Planade, R. Prototype of a Phosphine Sensor Based on a Conducting LB Film. *Sens. Actuators B Chem.* **1993**, *14* (1-3), 711-712. https://doi.org/10.1016/0925-4005(93)85154-3.
(16) Wu, J.-K.; Wu, E.-K.; Kim, N.-Y.; Kim, E.-S.; Gu, X.-F.; Liang, J.-G. Operation Temperature Effects on a Microwave Gas Sensor with and without Sensitive Material. *ACS Sens.* **2024**, *9* (9), 4731-4739. https://doi.org/10.1021/acssensors.4c01108.
(17) He, L.; Lv, H.; Ma, L.; Li, W.; Si, J.; Ikram, M.; Ullah, M.; Wu, H.; Wang, R.; Shi, K. Controllable Synthesis of Intercalated γ-Bi_2MoO_6/Graphene Nanosheet Composites for High Performance NO_2 Gas Sensor at Room Temperature. *Carbon* **2020**, *157*, 22-32. https://doi.org/10.1016/j.carbon.2019.10.011.
(18) Zhang, C.; He, X.; Zhou, Y.; Xu, J.; Zheng, Z.; Bian, Y.; Debliquy, M. Highly Sensitive and Stable Yolk-Shell Bi_2MoO_6 Gas Sensor for Ppb-Level Isopropanol Detection. *Sens. Actuators B Chem.* **2024**, *401*, 135059. https://doi.org/10.1016/j.snb.2023.135059.
(19) Li, B.; Lai, C.; Zhang, M.; Liu, S.; Yi, H.; Liu, X.; An, N.; Zhou, X.; Li, L.; Fu, Y.; Qin, L.; Chen, L. N, S-GQDs and Au Nanoparticles Co-Modified Ultrathin Bi_2MoO_6 Nanosheet with Enhanced Charge Transport Dynamics for Full-Spectrum-Light-Driven Molecular Oxygen Activation. *Chem. Eng. J.* **2021**, *409*, 128281. https://doi.org/10.1016/j.cej.2020.128281.
(20) Narwade, S. H.; Shinde, P. V.; Shinde, N. M.; Jadhav, V. V.; Shaikh, S. F.; Mane, R. S.; Bhosle, U. V. Hydrangea-Type Bismuth Molybdate as a Room-Temperature Smoke and Humidity Sensor. *Sens. Actuators B Chem.* **2021**, *348*, 130643. https://doi.org/10.1016/j.snb.2021.130643.
(21) Zhang, F.; Xu, Y.; Zhang, X.; Sui, L.; Hu, P.; Zheng, Z.; Cheng, X.; Gao, S.; Zhao, H.; Huo, L. Highly Selective Ppb-Level H_2S Sensor Based on the Walnut-like Bi_2MoO_6 at Low Temperature. *Sens. Actuators B Chem.* **2018**, *277*, 312-319. https://doi.org/10.1016/j.snb.2018.08.151.
(22) Li, J.; Liu, X.; Sun, Z.; Pan, L. Mesoporous Yolk-Shell Structure Bi_2MoO_6 Microspheres with Enhanced Visible Light Photocatalytic Activity. *Ceram. Int.* **2015**, *41* (7), 8592-8598. https://doi.org/10.1016/j.ceramint.2015.03.068.

(23) Liu, S.; Qin, Y.; Xie, J. Tuning Reactivity of Bi_2MoO_6 Nanosheets Sensors toward NH_3 via Ag Doping and Nanoparticle Modification. *J. Colloid Interface Sci.* **2022**, *625*, 879-889. https://doi.org/10.1016/j.jcis.2022.06.026.
(24) Zhang, Q.; Ma, S.; Liu, W.; Yuan, F.; Alhadi, A. Significant Butanol Gas Sensor Based on Unique Bi_2MoO_6 Porous Microspheres and ZnO Nanosheets Composite Nanomaterials. *J. Alloys Compd.* **2022**, *911*, 164877. https://doi.org/10.1016/j.jallcom.2022.164877.
(25) Zhang, F.; Xu, Y.; Zhang, X.; Sui, L.; Hu, P.; Zheng, Z.; Cheng, X.; Gao, S.; Zhao, H.; Huo, L. Highly Selective Ppb-Level H2S Sensor Based on the Walnut-like Bi_2MoO_6 at Low Temperature. *Sens. Actuators B Chem.* **2018**, *277*, 312-319. https://doi.org/10.1016/j.snb.2018.08.151.
(26) Wang, Z.; Li, P.; Feng, B.; Feng, Y.; Cheng, D.; Wei, J. Wireless Gas Sensor Based on the Mesoporous ZnO-SnO_2 Heterostructure Enables Ultrasensitive and Rapid Detection of 3-Methylbutyraldehyde. *ACS Sens.* **2024**, *9* (5), 2585-2595. https://doi.org/10.1021/acssensors.4c00306.
(27) Fang, W. Q.; Yang, X. H.; Zhu, H.; Li, Z.; Zhao, H.; Yao, X.; Yang, H. G. Yolk@shell Anatase TiO_2 Hierarchical Microspheres with Exposed {001} Facets for High-Performance Dye Sensitized Solar Cells. *J. Mater. Chem.* **2012**, *22* (41), 22082. https://doi.org/10.1039/c2jm34787c.
(28) Wu, K.; Chai, H.; Xu, K.; Debliquy, M.; Zhang, C. Effect of {010} Crystal Facets of Bi_2MoO_6 and 1D/2D Heterostructures for Conductometric Room Temperature NH_3 Gas Sensors. *Sens. Actuators B Chem.* **2023**, *376*, 132983. https://doi.org/10.1016/j.snb.2022.132983.
(29) He, X.-X.; Chai, H.-F.; Zhou, Y.-W.; Liu, K.-W.; Yu, Z.-X.; Zhang, C. Sensing Properties and Mechanisms of LaF_3-Co_3O_4 Nanorods for Low-Concentration Methanol Detection. *Rare Met.* **2024**, *43* (5), 2193-2204. https://doi.org/10.1007/s12598-023-02593-6.
(30) Zhang, Q.; Ma, S.; Liu, W.; Yuan, F.; Alhadi, A. Significant Butanol Gas Sensor Based on Unique Bi_2MoO_6 Porous Microspheres and ZnO Nanosheets Composite Nanomaterials. *J. Alloys Compd.* **2022**, *911*, 164877. https://doi.org/10.1016/j.jallcom.2022.164877.
(31) Huang, X.; Chen, K.; Xie, W.; Li, Y.; Yang, F.; Deng, Y.; Li, J.; Jiang, F.; Shu, Y.; Wu, L.; Xie, W.; Deng, Y. Chemiresistive Gas Sensors Based on Highly Permeable Sn-Doped Bismuth Subcarbonate Microspheres: Facile Synthesis, Sensing Performance, and Mechanism Study. *Adv. Funct. Mater.* **2023**, *33* (45), 2304718. https://doi.org/10.1002/adfm.202304718.
(32) Li, S.; Wang, C.; Liu, Y.; Cai, M.; Wang, Y.; Zhang, H.; Guo, Y.; Zhao, W.; Wang, Z.; Chen, X. Photocatalytic Degradation of Tetracycline Antibiotic by a Novel $Bi_2Sn_2O_7$/Bi_2MoO_6 S-Scheme Heterojunction: Performance, Mechanism Insight and Toxicity Assessment. *Chem. Eng. J.* **2022**, *429*, 132519. https://doi.org/10.1016/j.cej.2021.132519.
(33) Yu, T.; Li, Z.; Chen, S.; Ding, Y.; Chen, W.; Liu, X.; Huang, Y.; Kong, F. Facile Synthesis of Flowerlike Bi_2MoO_6 Hollow Microspheres for High-Performance Supercapacitors. *ACS Sustain. Chem. Eng.* **2018**, *6* (6), 7355-7361. https://doi.org/10.1021/acssuschemeng.7b04673.
(34) Wang, C.; Cui, X.; Liu, J.; Zhou, X.; Cheng, X.; Sun, P.; Hu, X.; Li, X.; Zheng, J.; Lu, G. Design of Superior Ethanol Gas Sensor Based on Al-Doped NiO Nanorod-Flowers. *ACS Sens.* **2016**, *1* (2), 131-136. https://doi.org/10.1021/acssensors.5b00123.

(35) Pan, J.; Chu, J.; Zhang, L.; Bo, K.; Yang, A.; Yuan, H.; Rong, M.; Wang, X. Bi_2O_3 Nanosheets for Early Warning Thermal Runaway of Lithium Battery. *Adv. Funct. Mater. n/a* (n/a), 2407408. https://doi.org/10.1002/adfm.202407408.
(36) Kim, K.; Pornaroontham, P.; Choi, P. G.; Itoh, T.; Masuda, Y. Self-Adaptive Gas Sensor System Based on Operating Conditions Using Data Prediction. *ACS Sens.* **2022**, *7* (1), 142-150. https://doi.org/10.1021/acssensors.1c01864.
(37) Shan, Z.; Xiao, J.; Wu, M.; Wang, J.; Su, J.; Yao, M.; Lu, M.; Wang, R.; Zhang, G. Topologically Tunable Conjugated Metal-Organic Frameworks for Modulating Conductivity and Chemiresistive Properties for NH_3 Sensing. *Angew. Chem. Int. Ed.* **2024**, *63* (16), e202401679. https://doi.org/10.1002/anie.202401679.
(38) Tang, W.; Chen, Z.; Song, Z.; Wang, C.; Wan, Z.; Chan, C. L. J.; Chen, Z.; Ye, W.; Fan, Z. Microheater Integrated Nanotube Array Gas Sensor for Parts-Per-Trillion Level Gas Detection and Single Sensor-Based Gas Discrimination. *ACS Nano* **2022**, *16* (7), 10968-10978. https://doi.org/10.1021/acsnano.2c03372.
(39) Xu, J.; Zhang, C. Oxygen Vacancy Engineering on Cerium Oxide Nanowires for Room-Temperature Linalool Detection in Rice Aging. *J. Adv. Ceram.* **2022**, *11* (10), 1559-1570. https://doi.org/10.1007/s40145-022-0629-8.
(40) Eguchi, K.; Cauhape, J. S.; Menil, F.; Lucat, C.; Videau, J. J. Detection of Phosphine with Semiconductive Fe_2O_3 Thick Films: Comparison with Other Binary Oxides. *Sens. Actuators* **1989**, *17* (1-2), 319-325. https://doi.org/10.1016/0250-6874(89)80097-6.
(41) Ozdemir, S.; Gole, J. L. A Phosphine Detection Matrix Using Nanostructure Modified Porous Silicon Gas Sensors. *Sens. Actuators B Chem.* **2010**, *151* (1), 274-280. https://doi.org/10.1016/j.snb.2010.08.016.
(42) Ozdemir, S.; Gole, J. L. Porous Silicon Gas Sensors for Room Temperature Detection of Ammonia and Phosphine. *ECS Trans.* **2008**, *16* (11), 379-385. https://doi.org/10.1149/1.2981142.
(43) Zhang, S.; Pu, W.; Chen, A.; Xu, Y.; Wang, Y.; Yang, C.; Gong, J. Oxygen Vacancies Enhanced Photocatalytic Activity towards VOCs Oxidation over Pt Deposited Bi_2WO_6 under Visible Light. *J. Hazard. Mater.* **2020**, *384*, 121478. https://doi.org/10.1016/j.jhazmat.2019.121478.
(44) Qin, Y.; Liu, S.; Shen, X.; Gui, H.; Bai, Y. Enhanced Gas Sensing Performance of Bi_2MoO_6 with Introduction of Oxygen Vacancy: Coupling of Experiments and First-Principles Calculations. *J. Alloys Compd.* **2022**, *894*, 162534. https://doi.org/10.1016/j.jallcom.2021.162534.
(45) Liu, B.; Liu, Q.; Pang, Y.; Duan, Y.; Zhao, C. Antioxidant Sulfide-Linked Polymer Membrane with Inherent Microporosity Enables Fuel Cells to Achieve Outstanding Power Density and Durability Over a Wide Temperature Range. *Adv. Funct. Mater. n/a* (n/a), 2408291. https://doi.org/10.1002/adfm.202408291.
(46) Zhang, S.; Chang, X.; Zhou, L.; Liu, X.; Zhang, J. Stabilizing Single-Atom Pt on Fe_2O_3 Nanosheets by Constructing Oxygen Vacancies for Ultrafast H_2 Sensing. *ACS Sens.* **2024**, *9* (4), 2101-2109. https://doi.org/10.1021/acssensors.4c00162.
(47) Wang, C.; Chang, X.; Liu, X.; Zhang, J. $ZnIn_2S_4$ Nanosheets for Efficient NO_2 Detection

at Room Temperature: Insights into the Role of Sulfur Vacancies. *J. Phys. Chem. Lett.* **2024**, *15* (22), 5875-5882. https://doi.org/10.1021/acs.jpclett.4c00919.
(48) Cao, L.; Li, Y.; Huo, Y.; Sun, L.; Li, X.; Chen, L.; Yang, X.; Yuan, F.; Yao, M. Volatolomics in Fritillarias and Their Identification by Orientation Controlled cMOF Thin Film Chemiresistors. *Chin. J. Chem.* **2025**, *43* (4), 371-377. https://doi.org/10.1002/cjoc.202400883.
(49) Quan, W.; Shi, J.; Luo, H.; Fan, C.; Lv, W.; Chen, X.; Zeng, M.; Yang, J.; Hu, N.; Su, Y.; Wei, H.; Yang, Z. Fully Flexible MXene-Based Gas Sensor on Paper for Highly Sensitive Room-Temperature Nitrogen Dioxide Detection. *ACS Sens.* **2023**, *8* (1), 103-113. https://doi.org/10.1021/acssensors.2c01748.

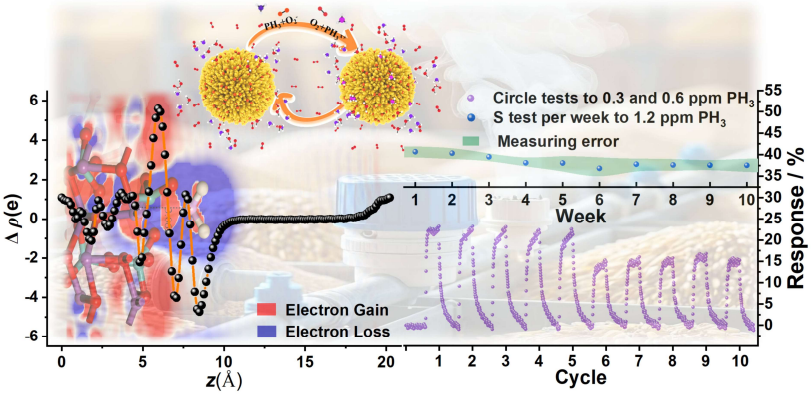

TOC graphics